Isolating and Quantifying Cross-Beam Energy Transfer in Direct-Drive Implosions on OMEGA and the National Ignition Facility

Introduction

In direct-drive inertial confinement fusion (ICF) experiments, laser beams directly illuminate a spherical capsule to drive an implosion. The capsule compression transfers the kinetic energy of the converging shell into the internal energy of the fuel, triggering fusion reactions in the hot dense core.[1] The laser energy that drives the implosion is absorbed in the plasma corona and conducted to the ablation front of the target by electron thermal transport, resulting into ablation of the shell and its corresponding acceleration caused by the rocket effect.[2]

Laser beams crossing in the coronal plasma can drive the stimulated Brillouin scattering (SBS) instability, which can redirect a significant fraction of the incident energy out of the plasma.[3] Cross-beam energy transfer (CBET) is seeded SBS facilitated by ion-acoustic waves driven by the beating of two electromagnetic waves in a plasma.[4] Depending on the amplitude of the driven ion-acoustic wave, energy is transferred from one electromagnetic (pump) wave to another (seed) wave. In direct-drive fusion experiments, outgoing rays that have refracted around the target beat with incoming rays from other beams to transfer significant energy out of the plasma before it can be absorbed. In simulations of direct-drive implosions, where individual beam intensities remain low ($I < 10^{14}$ W/cm^2), the amplitudes of the ion-acoustic waves are small. Nevertheless, significant energy transfer results from the net effect of many beam crossings throughout the coronal plasma.[5–7]

The existence of CBET was first demonstrated by experiments using planar targets.[8,9] In indirect-drive ICF experiments, this mechanism was used to transfer kilojoules of laser energy from the polar to the equatorial drive of an imploding target to improve capsule symmetry,[10–12] but uncertain plasma conditions and the large amplitude of the ion-acoustic waves driven by high single-beam intensities ($I \sim 10^{15}$ W/cm^2) have challenged the ability to obtain an accurate predictive model.[11–13] These experiments additionally identified the ability of CBET to rotate the polarization of the beams, suggesting that polarization rotation should be included when modeling systems with multiple CBET regions.[14,15] Direct-drive experiments used scattered-light spectra and shell-trajectory measurements to demonstrate the existence of CBET[5] and estimate its level.[6,16,17]

This article presents measurements of CBET's effect on coupling laser energy to the ablation front of a target by comparing its effect on the mass ablation rate and ablation-front trajectory in low- and high-CBET regions in the same implosion. A polar-direct-drive configuration[18] was used, in which a ring of beams encircling the equator was dropped and the remaining beams were repointed toward the equator, reducing detrimental CBET at the poles while enhancing it at the equator.[19,20] This combination of low- and high-CBET conditions in the same target implosion made it possible to determine the effects of CBET on hydrodynamic coupling (Fig. 146.1). The simultaneous measurements of the angularly resolved mass ablation rates and shell trajectories determine the kinetic energy of the implosion by providing the instantaneous mass of the target and the ablation-front velocity.

Two-dimensional *DRACO*[21] hydrodynamic simulations performed with an implicit Schurtz–Nicolai–Busquet (iSNB)

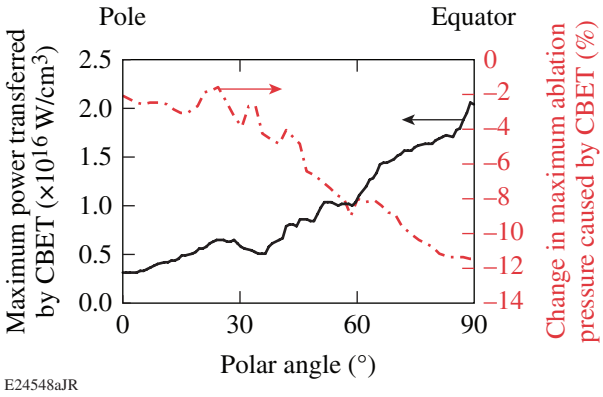

Figure 146.1
The polar-direct-drive laser configuration results in greater power transferred by cross-beam energy transfer (CBET) at the target equator compared to the pole (black curve). The consequent difference in ablation pressure (red dashed–dotted curve) was calculated from 2-D *DRACO* simulations with and without the CBET model for the highest-intensity polar-direct-drive OMEGA experiments (t = 0.8 ns).

thermal-transport model,[22] but without a CBET model, reproduced the measured trajectories at the pole of the target, verifying that the coupling physics is well modeled when CBET effects are negligible. These simulations, however, overpredicted the velocity of the shell and ablation rate at the equator. By including a 3-D ray-based CBET model adapted from 1-D plane-wave equations developed by Randall[4] in the hydrodynamic simulations, the simulated equatorial trajectories agreed better with measurements, while having a minimal impact on the polar trajectory. However, the simulations still overpredicted the drive at the equator.

The geometric ray-propagation model used in *DRACO* transports energy while neglecting diffraction effects that produce small-scale structures (temporal and spatial). The CBET model requires knowledge of the cumulative background pump intensity distributed over the propagation angle and wavelength, which is computed by accumulating the ray-energy path-length product and weighting the sum by the cell volume to capture the relevant hydrodynamic scale.[23] Diffraction may vary the energy transfer above or below the average value computed using this ray model if there is a nonlinear CBET response, but the net effect is uncertain given the small spatial and temporal interaction scales involved. *DRACO*'s ray model does not currently track polarization, but the net effect should be captured by assuming an even mixture, given the even distribution of polarization states generated by the polarization smoothing[24] processes on OMEGA.The correct formulation of the net response of polarization, which depends on the ray-interaction angles, is under investigation and may partially account for the overestimated shell kinetic energy. When a multiplier on the CBET gain was added to the model, excellent agreement between the measured and simulated mass ablation rates and shell trajectories was obtained at all angles. These measurements were performed on OMEGA[25] and at the National Ignition Facility (NIF)[26] to access a wide range of laser intensities, plasma conditions, and laser-beam geometries. The need for the CBET multiplier in all the tested configurations suggests that additional physics effects, such as diffraction, polarization effects, or shortcomings of extending the Randall model to 3-D, should be explored to explain the difference in observed and predicted drives.

Experimental Setup

1. Target and Laser Configuration

a. Isolating CBET. Experiments were performed on OMEGA[25] using forty 351-nm laser beams with equal energies, arranged in the polar-direct-drive configuration, with three rings of beams around each pole of the target chamber. The beams were repointed toward the target equator by 5° for the two inner rings of beams and 20° for the outer ring at each pole, using the angle definitions and pointing description from Ref. 27. The beam profiles were shaped with distributed phase plates[28] that provided second-order super-Gaussian laser spots on target (1/*e* radius of 183 μm). Two-dimensional smoothing by spectral dispersion (SSD)[29] and polarization smoothing[24] were used to treat the laser-intensity profiles. The laser pulses consisted of a 0.7-ns foot, ramping up to a 0.6-ns square pulse that drove the target to its final velocity (Fig. 146.2). The total energy on target was varied among 8.1±0.2 kJ ($I \approx 7 \times 10^{14}$ W/cm^2, where I is the peak overlapped intensity defined as the maximum power during the laser pulse divided by the initial surface area of the target), 11.8±0.1 kJ ($I \approx 10 \times 10^{14}$ W/cm^2), and 16.0±0.1 kJ ($I \approx 14 \times 10^{14}$ W/cm^2). The targets were 19.6±0.3-μm-thick spherical CH shells. They were coated with 2.4±0.2, 1.6±0.2, and 0.6±0.2-μm layers of Si, with outer diameters of 639 μm, known to ±1 μm with a variation between experiments of ±4 μm. The density of the Si coating was 2.1±0.2 g/cm^3 but had a significantly smaller variation (<0.2 g/cm^3) within a particular target batch. Each experimental configuration discussed here used targets from a single batch, so the density variation for a particular configuration was negligible.

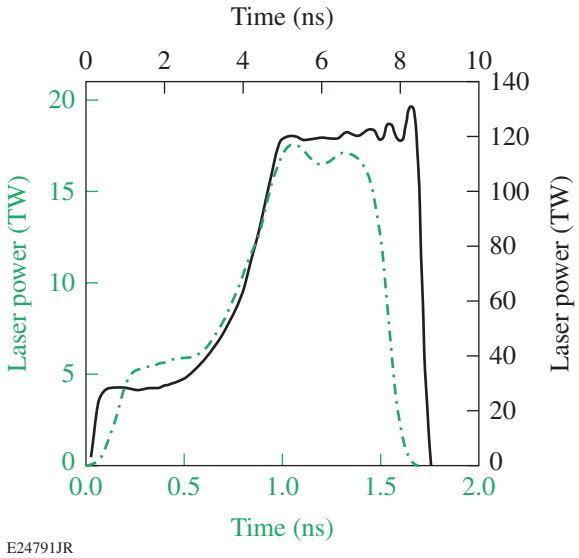

Figure 146.2
The laser pulse shapes are shown for the OMEGA (green dashed–dotted curve) and NIF (black solid curve) experiments.

b. Scaling to ignition conditions. Experiments were performed on the NIF using 192 laser beams (with one beam missing on the 2.5-μm Si experiment) in the indirect-drive configuration, with the polar-direct-drive beam-pointing design

and ring energies described in Ref. 30. This pointing design produced a round CH implosion in simulations when CBET was considered without a gain multiplier. The total laser energy was 660 kJ, giving a peak overlapped intensity on target of $\sim 8 \times 10^{14}$ W/cm^2.

The laser pulse was similar in shape to the OMEGA pulse but extended over 8 ns (Fig. 146.2). Targets were 90±2-μm-thick CH shells with Si coatings of 2.5±0.1 μm and 5±0.1 μm and outer diameters of 2314±2 μm. The density of the Si coating was reported as 2.1±0.2 g/cm^3.

c. Symmetric direct drive on OMEGA. Symmetric direct-drive experiments were performed on OMEGA using all 60 laser beams centered on the target. The same beam-smoothing methods, phase plates, pulse shape, total energies, and intensities were used as in the polar-direct-drive experiments. The targets were also similar to those used in the polar-direct-drive experiments, with 20.1±0.3-μm-thick CH shells having a variation between targets of ±0.8 μm and Si thicknesses of 2.4±0.2, 1.4±0.2, and 0.7±0.2 μm. Outer diameters had an average value of 637 μm, measured to ±2 μm, and a variation between targets of ±11 μm. The density of the Si coating was reported as 2.1±0.2 g/cm^3.

2. Self-Emission Diagnostic

a. Configuration of the x-ray framing camera. The x-ray self-emission was measured using four-strip x-ray framing cameras.[31,32] Two-dimensional images of the coronal x rays were formed using arrays of pinholes (8-μm diameter for OMEGA, 25-μm diameter for the NIF), placed to give 6× magnifications on OMEGA and 2× on the NIF. The ~50-ps time-gated images (~100 ps for the NIF) were taken throughout the implosion, with absolute timing known to ±10 ps and the interstrip timing of ~250 ps known to ±3 ps (Ref. 33). Five filters were used for the images throughout the course of the experiments: (1) 25 μm of Be, (2) 250 μm of Be, (3) 25 μm of Be with 23 μm of Saran, (4) 25 μm of Be with 50 μm of Kapton, and (5) 25 μm of Be with 75 μm of Kapton. Different filters were used to optimize imaging of the ablation front and the interface between the Si and CH in the corona. The 25-μm Be filter (blocking x rays <1 keV) was found to optimally image the CH ablation front late in time because of the lower ablation-front temperature. The 250-μm Be filter (blocking x rays <2 keV) was optimized to image the Si/CH interface as it expanded away from the ablation front because of the higher temperature in the corona. The combination of Be and Saran (blocking x rays <1.6 keV) provided a good compromise between the two. The Be and Kapton filters (blocking x rays <2 keV) were used on the NIF for the first three strips on each camera. Only 25 μm of Be was used for the last strip in each camera to measure the CH ablation-front position. Images were taken from the equator and pole for all of the polar-direct-drive experiments, so that both the variation in ablation rate and ablation-front trajectory with polar angle and the azimuthal symmetry of the implosion could be observed. Both configurations on OMEGA experiments had two equatorial cameras offset by 11° in polar angle from the equator and one camera on the pole to measure the azimuthal symmetry. The NIF experiments had one camera on the equator and one on the pole.

b. Trajectory measurements. X-ray self-emission images of Si-coated CH target implosions were used to determine the mass ablation rate of Si and the ablation-front trajectory of the target.[34,35] While the laser is on, the coronal plasma around the target is continually heated and emits soft x rays. The x-ray intensity that is line integrated through the target is imaged through a pinhole onto a time-gating diagnostic plane. Figure 146.3 shows the x-ray self-emission technique at a time shortly after the laser burned through the Si layer of the target, when the corona consists of an outer Si plasma and an inner CH plasma surrounding the unablated target.

Figure 146.3(b) shows the simulated x-ray intensity profile at the diagnostic plane when two distinct features are observed. Moving from the outside of the plasma toward the target center, an increase in x-ray intensity is observed as the line-integrated distance through the Si plasma increases. A rapid drop in intensity occurs at the interface between the Si and CH as the lower-emitting CH quickly dominates the integrated x-ray emission region (outer feature). The intensity again increases with further progress toward the center of the target until the ablation front is reached. At the ablation front, the emission quickly drops because the shell is optically thick (inner feature). These two features observed in the radial intensity at the diagnostic plane are used to track the positions of the Si/CH interface and ablation front.[35]

Figure 146.4 shows measured x-ray self-emission images and their respective intensity profiles at three different times for a symmetrically illuminated implosion. In the symmetric images, these profiles are angularly averaged around 360° of the image to obtain a measurement accurate to <1 μm for both the inner gradient (ablation-front radius) and outer peak locations (Si/CH interface position). In angularly resolved images, the profiles at the pole and equator are each averaged over 40° (20° at each pole or each side of the equator). The instrument function of the x-ray diagnostic (defined predominantly by the pinhole size)

introduced a small systematic shift (~2 μm) between the position of the inner gradient and the actual position of the ablation front.[35] This shift was determined by post-processing simulations with *Spect3D*[36] and convolving with the instrument function to calculate self-emission images. The shifts are known to ±1 μm for the ablation front and ±2 μm for the Si/CH interface.

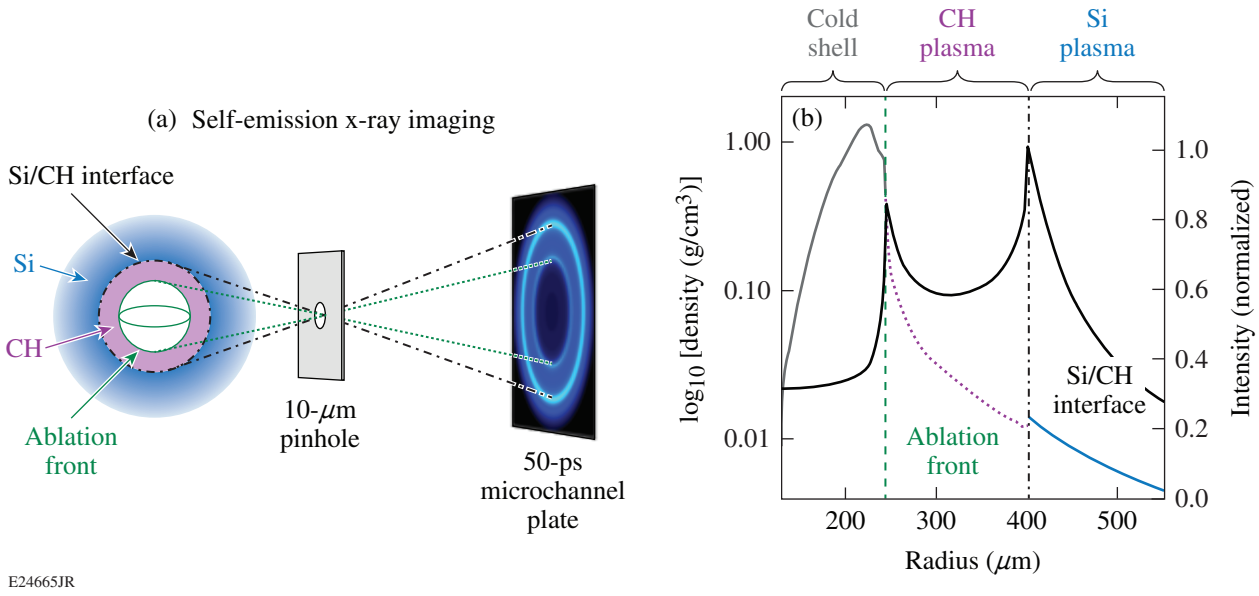

Figure 146.3

(a) Line-integrated x-ray self-emission from the target is imaged through a pinhole and filter (transmits >1 keV) onto an ~50-ps time-gated microchannel plate. (b) Comparison of the calculated radial x-ray intensity profile measured at the diagnostic plane (black solid curve) with the simulated target-density profile in the cold shell (gray solid curve), in the CH plasma (purple dotted curve), and in the Si plasma (blue solid curve). Two peaks in the emission correspond to the positions of the Si/CH interface in the coronal plasma (black dashed–dotted line) and the ablation front of the imploding shell (green dashed line). No instrument function is included in the x-ray intensity profile calculation to illustrate the steep gradients at the ablation surface and Si/CH interface.

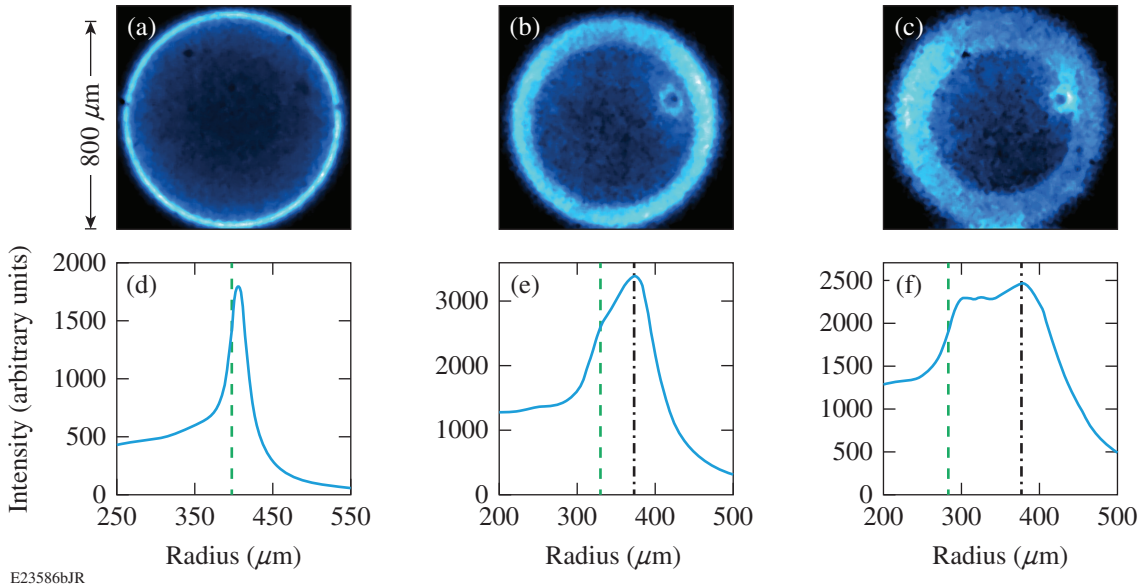

Figure 146.4

Self-emission x-ray images, taken (a) before and [(b),(c)] at two different times shortly after the laser burns through the Si layer, are shown with their corresponding averaged radial profiles. The positions of the measured ablation front (green dashed line) and the Si/CH interface (black dashed–dotted line) are included.

c. Measurements of mass ablation rate. The average mass ablation rate of the Si from the start of the laser pulse to the Si burnthrough time is determined by dividing the total ablated mass (calculated from the initial Si mass) by the time it took the laser to burn through the Si layer. The time-resolved mass ablation rate was determined by varying the thickness of the Si outer layer to determine the time-averaged mass ablation rate at different times during the implosion.

To determine the burnthrough time in each experiment, the measured Si/CH interface and ablation-front positions from the series of images taken for a particular implosion were plotted to generate the ablation-front and Si/CH interface trajectories. The burnthrough time of the Si layer corresponds to the time when the Si/CH interface trajectory separates from the ablation-front trajectory. To accurately determine the burnthrough time, a range of simulations was performed, varying the CBET multiplier. The simulation that simultaneously reproduced both measured trajectories was used to determine the Si burnthrough times around the target. The accuracy of the measurement corresponds to the variation in the burnthrough time for the simulated trajectories that are within the error bars of the experimental measurements.

The Si/CH interface trajectory is sensitive to the initial Si mass. For all experiments in a given target batch, the optimum Si density used in the simulations was determined by finding the density that minimized the differences between the simulated and measured interface trajectories at the pole. The density was varied within the measurement uncertainties (see **Isolating CBET**, below). The absolute error in the mass largely results from the uncertainty in density. This inaccuracy in the calculated mass could mask uncertainties in the equation of state, opacity, and thermal-transport models, but tests show that these effects primarily act symmetrically. Any changes in the models that affect the trajectories symmetrically must be offset by changes in another symmetric coupling model—not the CBET model—to maintain agreement with the measured polar trajectories.

Experiments

1. Isolating CBET

To measure the effects of CBET in direct-drive experiments on OMEGA, a laser configuration was used in which a ring of beams around the equator was turned off and the remaining beams were repointed toward the equator. This configuration limits the intensity of the refracted outgoing light that interacts with incoming polar beams, significantly reducing CBET at the pole. The repointing increases the flux of unabsorbed light propagating through the equatorial coronal plasma, which enhances CBET at the equator (Fig. 146.1). The implosions were designed to have nearly uniform drive around the target when CBET was not taken into consideration, so differences in measured drive between the pole and equator are attributed to CBET.

Figure 146.5 shows x-ray self-emission images taken from the equator after the laser burns through the Si layer. The intensity features visible in the images show the positions of the ablation front and Si/CH interface, which form two concentric ellipses with opposite ellipticity. The ablation-front ellipses show larger shell radii at the equator compared to the pole, demonstrating that the ablation pressure is lower at the equator compared to the pole. The smaller separations between the Si/CH interface and ablation-front ellipses at the equator,

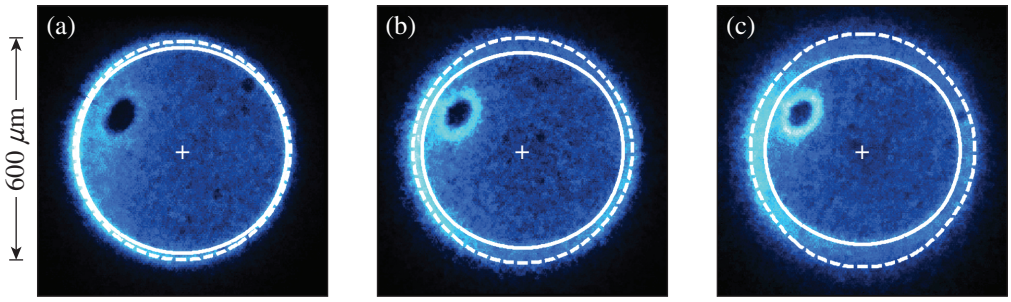

Figure 146.5
X-ray images taken after the burnthrough of a thin Si layer at (a) $t = 0.7$, (b) 0.8, and (c) 0.9 ns in an experiment having the highest intensity (14×10^{14} W/cm^2) are shown. The images indicate earlier burnthrough at the poles of the target (top and bottom of images) than at the equator. The increased separation of the Si/CH interface (dotted line) and ablation front (solid line) at the poles implies a greater time of expansion for the Si from the ablation front. This increased drive results in a smaller ablation-front radius measured at the pole than at the equator.

compared to the pole, indicate that the laser burned through the Si later at the equator. The expansion of the Si/CH interface away from the target and compression of the ablation front as a function of time can be seen through the series of images.

Figure 146.6 shows the ablation-front and interface trajectories used to determine the Si burnthrough times, i.e., the time that each trajectory pair separated with values of 0.59±0.04 ns for the equator and 0.52±0.04 ns for the pole. The later burnthrough time at the equator, compared to the pole, agrees with the lower mass ablation rate at the equator suggested by the individual images. The measured ablation-front radii of 140±2 μm for the equator and 111±2 μm for the pole at 1.49±0.01 ns indicate a lower average ablation pressure at the equator compared to the pole, which leads to a slower velocity.

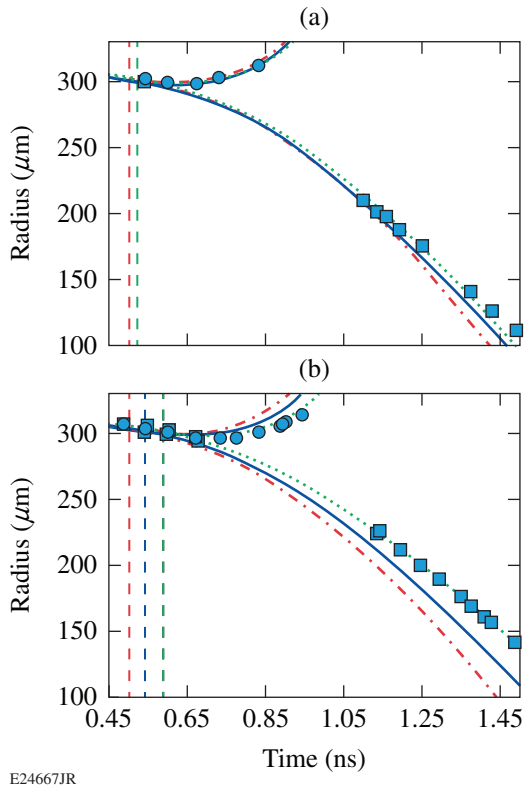

Figure 146.6
Measured Si/CH interface (blue circles) and ablation-front (blue squares) trajectories from three cameras are plotted for the (a) pole and (b) equator for the highest-intensity OMEGA polar-drive experiment with a 2.4-μm layer of Si. Error bars for the radius measurements are smaller than the data points (±2 μm for the ablation-front measurements and ±4 μm for the Si/CH interface measurements). Simulations performed with no CBET model (red dashed–dotted curve), the standard CBET model (blue solid curve), and the CBET model with the best-fitting gain multiplier (green dotted curve; $f_{\mathrm{CBET}} = 2.7$) are shown. The time that the laser burned through the Si in each simulation is marked with a dashed line of the corresponding color. Good agreement between the measurements and all models was obtained at the pole where CBET was minimal.

a. Comparison with hydrodynamic simulations. Figure 146.6 shows good agreement between the trajectory measurements at the pole and polar trajectories taken from *DRACO*[21] simulations that did not include CBET. This agreement at the pole suggests that the coupling physics is well modeled when CBET effects are small. Calculated trajectories at the equator are very similar to those calculated at the pole, which suggests that without CBET, the implosion would be symmetric. However, the measured equatorial trajectories show later burnthrough and a larger final radius than were calculated, indicating that the CBET significantly reduced the drive at this location.

A 3-D ray-based model[23] adapted from the 1-D Randall plane-wave equations[4] was implemented in *DRACO*. Figure 146.6 shows that simulations run with this model calculate a preferential decrease in drive at the equator, bringing simulations into better agreement with measurements. The addition of this CBET model results in small changes in the calculated polar trajectories at early times, verifying that CBET is negligible at the pole until the target radius is $\lesssim$250 μm (~0.9 ns). An increased effect of CBET at the pole is observed at this point because of an increase in the SBS seeds from rays that were previously shadowed by the target and an increase in the incident laser power (Fig. 146.2). Even late in time, however, the ablation-front trajectories calculated without CBET are in reasonable agreement with the measurements.

The trajectories at the equator are slowed to a greater degree than at the poles, indicating that CBET has a stronger effect at this location. The simulated Si burnthrough time is still too early and the ablation-front trajectory still too fast, however, to agree with the measurements. To estimate the CBET modification required to bring simulations into agreement with measurements, a multiplier (f_{CBET}) was incorporated into the CBET gain length:

$$L_{\mathrm{s}}^{-1} = f_{\mathrm{CBET}} \frac{k_0}{4} \frac{n_0}{\epsilon n_{\mathrm{c}}} \left(\frac{m v_q^2}{T_{\mathrm{e}}} \right) \times \left[\left(1 + \frac{3 T_{\mathrm{i}}}{Z T_{\mathrm{e}}} \right) \left(\frac{\nu_{\mathrm{i}}}{\omega_{\mathrm{s}}} \right) \right]^{-1} P(\eta), \quad (1)$$

given by Eq. (18) in Ref. 4, where all other parameters are defined within the reference.

Figure 146.6 shows that excellent agreement with the measurements was obtained when a multiplier of 2.6±0.3 was used. To determine the optimal multiplier, a χ^2 analysis was used to minimize the differences between measured and simulated trajectories (Fig. 146.7), where

$$\chi^2 = \sum_{i=1}^{N} \frac{1}{N} \frac{\left[r_i - x(t_i)\right]^2}{\sigma_{r_i}^2}, \tag{2}$$

and r_i is the measured position, $x(t_i)$ is the simulated radius, σ_{r_i} is the uncertainty in the experimental measurement (±2 μm for the ablation-front location and ±4 μm for the Si/CH interface position), and N is the total number of points measured. The error bar on the multiplier was determined from the uncertainty in absolute timing (±10 ps)—shifting the experimental image timing relative to the simulation gives an error bar on the multiplier of ±0.4 ps for high intensities to ±0.6 ps for each low-intensity experiment.

All of the simulations described here were performed using the code *DRACO* with the iSNB nonlocal thermal-transport model,[22] *SESAME* equation-of-state tables,[37] and collisional-radiative opacity tables.[38] The polar angle's dependence on the laser energy deposition, hydrodynamic efficiency, and thermal conduction is generated by the polar-direct-drive configuration, which invokes lateral thermal transport.

b. Intensity and Si-thickness scalings. Figure 146.7 shows measurements of the polar and equatorial trajectories for the 2.4-μm Si experiment at three intensities. For each intensity, simulations without CBET agreed well with experimental measurements at the pole, showing that the simulations reproduce

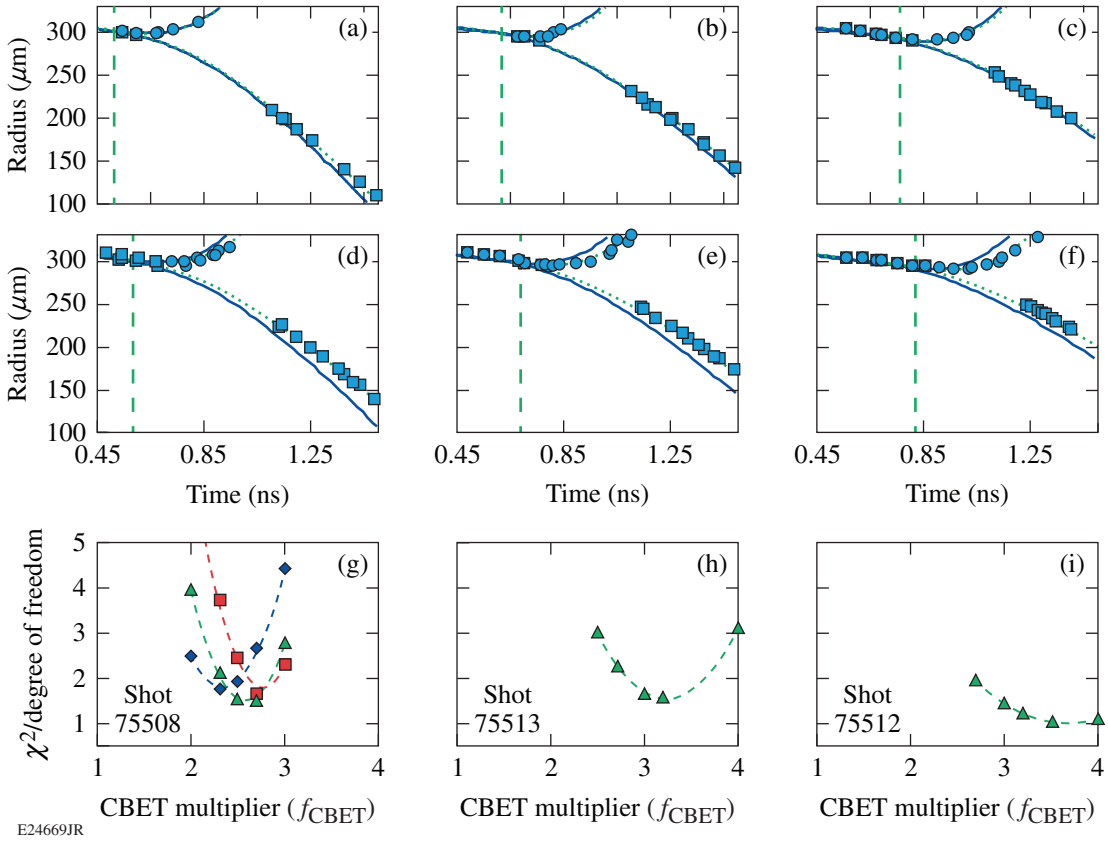

Figure 146.7
Comparison of the measured ablation front (blue squares) and Si/CH interface (blue circles) with simulated trajectories generated by *DRACO* with CBET using no multiplier (blue solid curves) and CBET with the best-fit multiplier (green dotted curves) for targets with 2.5 μm of Si. Included are trajectories for [(a)–(c)] the pole and [(d)–(f)] equator for $I = 14 \times 10^{14}$ W/cm^2 (left column), 10×10^{14} W/cm^2 (middle column), and 7×10^{14} W/cm^2 (right column). The Si burnthrough times are plotted (green dashed lines). The χ^2 minimization analyses are plotted for (g) $I = 14 \times 10^{14}$ W/cm^2, (h) 10×10^{14} W/cm^2, and (i) 7×10^{14} W/cm^2 to determine the optimal multiplier and error bars. For the highest intensity, the χ^2 values are shown for the optimal timing (green triangles), –10 ps (blue diamonds), and +10 ps (red squares). The possible error in the CBET multiplier is determined from the shift in the location of the minimum χ^2 with the uncertainty in the timing.

the hydrodynamic coupling when CBET is negligible, but the ablation rate and ablation-front velocity are overpredicted at the equator. With the introduction of the CBET model using the optimized multiplier, excellent agreement at both the pole and equator was found for each intensity. The optimized values of 2.8±0.5, 3.1±0.5, and 3.9±1.0 were determined for this configuration with overlap intensities of $I = 14 \times 10^{14}$ W/cm^2, 10×10^{14} W/cm^2, and 7×10^{14} W/cm^2, respectively. As the intensity decreases, the χ^2 curve broadens because of the smaller effect of CBET at lower intensities.

Figure 146.8 shows the mass-ablation-rate measurements at the pole and the equator for the highest laser-intensity experiments. The experiments were performed using three different thicknesses of the Si outer layer (0.6, 1.6, and 2.4 μm) to evaluate the average mass ablation rate of the Si at different times during the implosion. For three intensities, good agreement between simulated and experimental burnthrough times verifies the simulated time-resolved mass ablation rates taken when the optimal intensity multiplier was used.

2. Scaling to Ignition Conditions

Figure 146.9 shows the trajectory results from direct-drive experiments performed on the NIF to access ignition-relevant conditions (Table 146.I). The images taken during the NIF experiments were used to measure the ablation-front trajectories at the pole and the equator. Measured ablation-front trajectories agree well with simulations that used a CBET multiplier

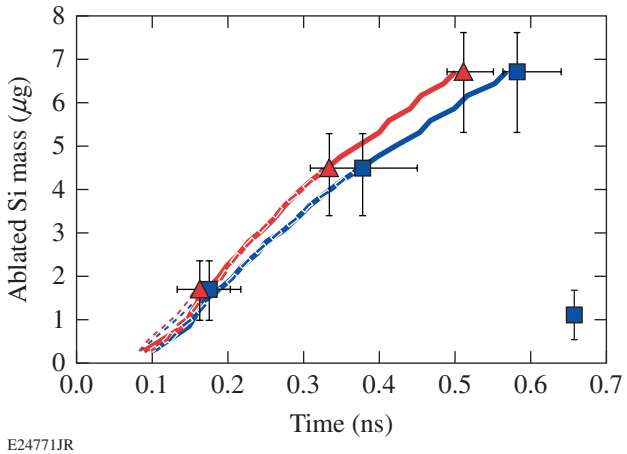

Figure 146.8
Ablated Si mass as a function of the measured burnthrough time at the pole (red triangles) and equator (blue squares) for a laser intensity of 14×10^{14} W/cm^2 is compared with simulations (dotted curve: 0.6 μm; dashed curve: 1.6 μm; and solid curve: 2.4 μm) using the optimal multipliers. The small shot-to-shot variations in the simulated ablation rate result from minor variations in the laser pulse and target size. Absolute error bars are shown for the Si mass. The relative error in mass (shown on the sample point in the lower right corner) is reduced because the density can be considered to be the same for all targets in a given batch.

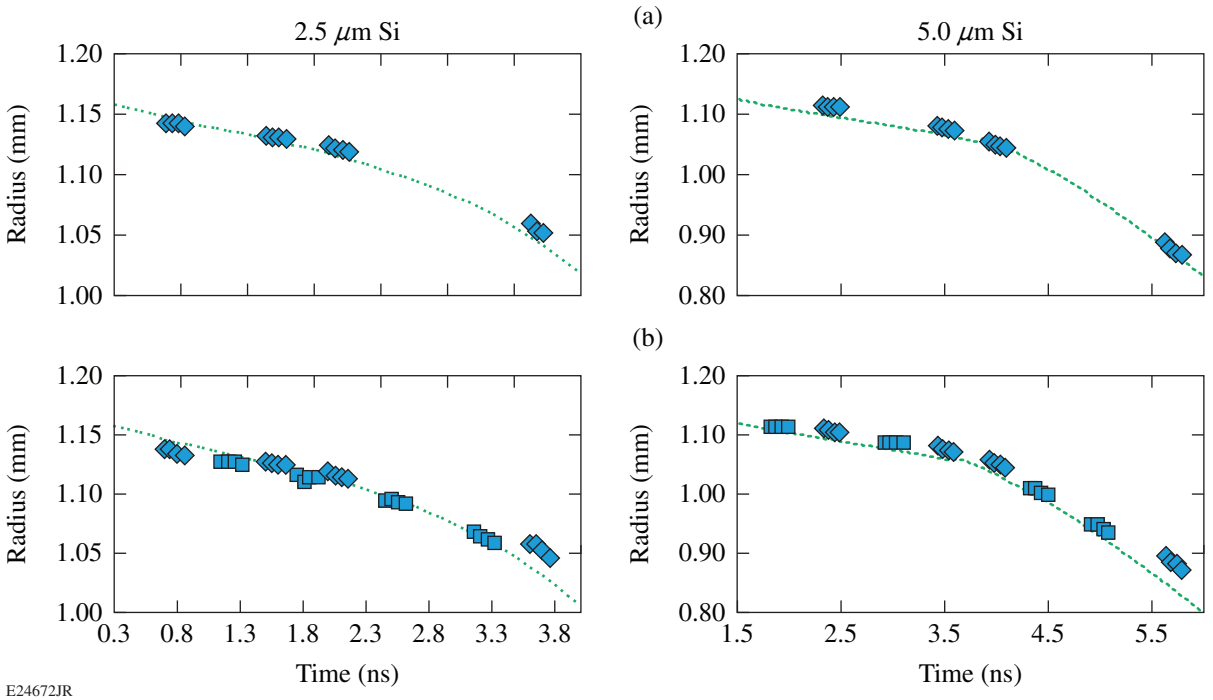

Figure 146.9
The measured ablation-front positions (blue squares) are compared with simulations (green dotted curves) for targets with [(a),(b)] 2.5 μm and [(c),(d)] 5 μm of Si at the [(a),(c)] pole and [(b),(d)] equator.

of 2, which has been shown for similar NIF experiments that used CH shells.[39] To mitigate the effects of shell decompression on the ablation-front trajectories, the experiments were limited to early times. Large perturbations at the ablation front can expand the ablation-front surface away from the shell's center of mass.[39] In the OMEGA experiments, the 2-D SSD limits the imprint, and perturbations were shown to have minimal impact on the trajectories.[35] At both facilities the radiation from the Si layer reduced the Rayleigh–Taylor (RT) growth, but on the NIF, the RT growth caused by high levels of laser imprint occurred in spite of the smoothing effects; this mixed the Si and CH at the interface, reducing the contrast of the outer interface peak in the x-ray images. As a result, the ability to measure the Si/CH interface trajectory on the NIF was limited.

Table 146.I: Comparison of the laser energy (E_L), electron temperature at the quarter-critical surface (T_e), density scale length (L_n), and overlap intensity at the quarter-critical surface (I_{qc}) near the end of the laser pulse for OMEGA and NIF polar-direct-drive experiments.

Parameter	OMEGA	NIF	Ignition
E_L	24 kJ	660 kJ	1500 kJ
T_e	2.7 keV	2.9 keV	4 keV
L_n	150 μm	350 μm	500 μm
I_{qc}	5×10^{14} W/cm^2	3×10^{14} W/cm^2	10^{15} W/cm^2

3. Symmetric Direct Drive on OMEGA

Figure 146.10 shows the trajectory results for symmetric direct-drive experiments on OMEGA. A CBET gain multiplier

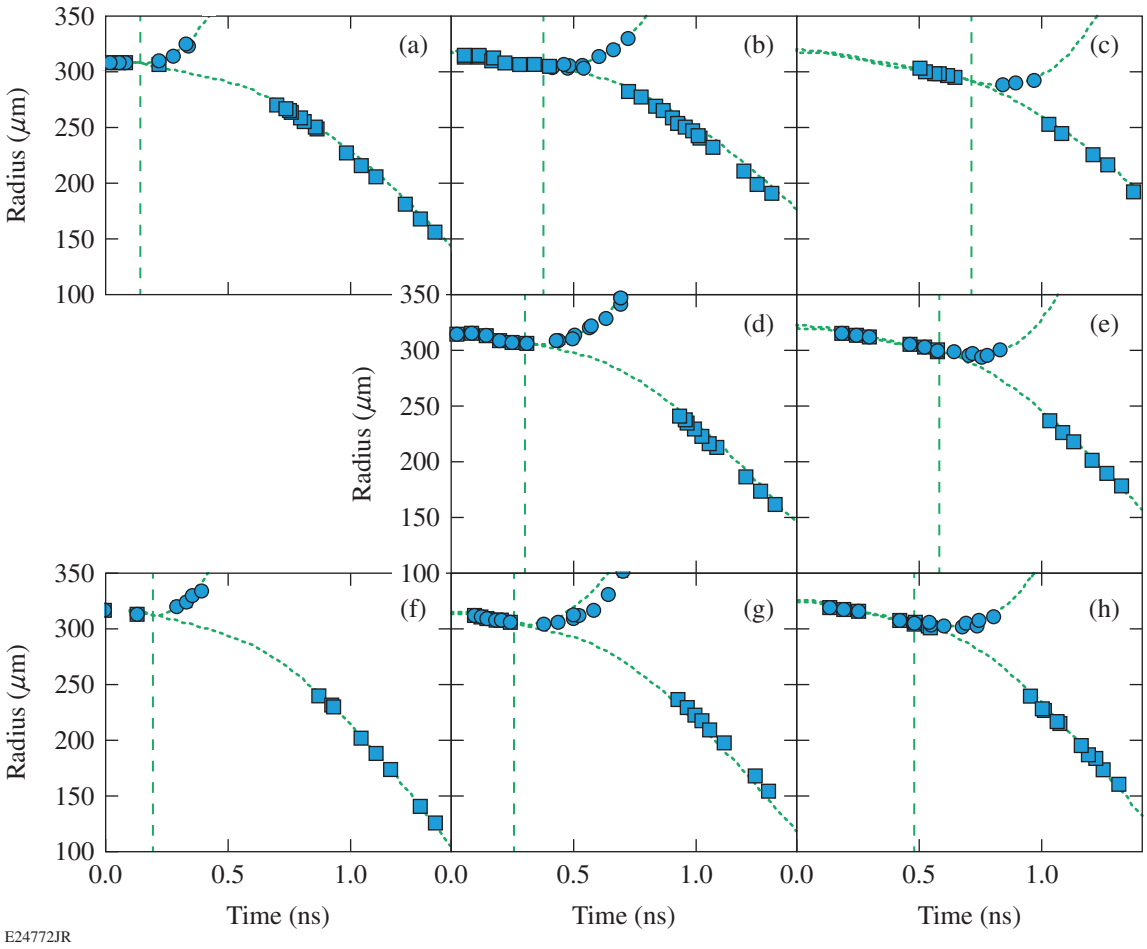

Figure 146.10
Comparison of the measured ablation-front (blue squares) and Si/CH interface (blue circles) positions with simulated trajectories (green dotted curve) for [(a)–(c)] $I = 7 \times 10^{14}$ W/cm^2; [(d),(e)] 10×10^{14} W/cm^2; and [(f)–(h)] 14×10^{14} W/cm^2 for targets with Si thicknesses of [(a),(f)] 0.7 μm; [(b),(d),(g)] 1.6 μm; and [(c),(e),(h)] 2.6 μm. The Si burnthrough times are plotted in the figure (green dashed lines).

of 2 was found to reproduce the trajectories and burnthrough times (mass ablation rates) for all combinations of laser intensity and Si thickness tested.

Conclusions

The CBET physics in direct-drive implosions was analyzed using simultaneous 2-D Si mass-ablation-rate and ablation-front-trajectory measurements. A polar-direct-drive configuration was employed, where beams were removed from the equator of a symmetrically illuminated target and the remaining beams were repointed toward the equator. This configuration suppressed CBET at the pole, while enhancing its effects at the equator. Implosion trajectories simulated without CBET were in good agreement with the measured polar trajectories for all conditions tested. This suggests that the other coupling physics is well modeled at the pole when CBET is small. The calculated mass ablation rates and ablation-front trajectories are in excellent agreement with the measurements at the pole and the equator when a 3-D ray-based CBET model is included in the simulations with a CBET gain multiplier. These measurements were performed on both OMEGA and the NIF to access a wide range of laser intensities, plasma conditions, and laser-beam geometries. The multiplier was necessary for all laser conditions, and the optimal multiplier for each configuration is shown in Fig. 146.11. The multiplier is constant for symmetric OMEGA experiments and decreases with increasing intensity in OMEGA polar-direct-drive implosions. The presence of the CBET gain multiplier required to match the data in all of the configurations tested suggests that additional physics effects should be explored, such as intensity variations caused by diffraction, polarization effects, or shortcomings of extending the 1-D Randall model to 3-D. The variation in the CBET multiplier in the polar-drive configuration, while it is constant in the symmetric configuration, suggests that additional physics may be affecting the polar-drive implosions. For example, the beams pointed toward the equator may experience increased CBET because of their increased interaction length. This increased transfer may saturate at high laser intensities, resulting in a decreasing CBET multiplier. Another candidate for further exploration is the effect of lateral thermal transport on the plasma conditions since the polar-drive configuration experiences lateral temperature gradients that do not exist in a symmetric configuration and the plasma conditions affect the level of energy transfer.

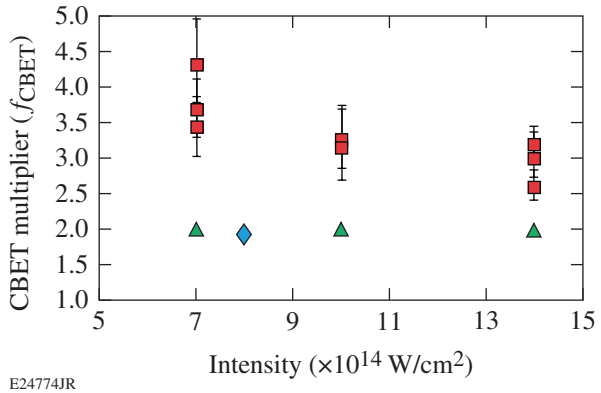

Figure 146.11
CBET multipliers that minimize the χ^2 difference between simulations and measurements are shown as a function of peak laser intensity for OMEGA symmetric direct-drive (green triangles) and polar-direct-drive (red squares) experiments and NIF experiments (blue diamond).

ACKNOWLEDGMENT

The authors thank the operations teams at both the Omega Laser Facility and the National Ignition Facility for their outstanding work. This work was supported by the U.S. Department of Energy Office of Inertial Confinement Fusion under Award Number DE-NA0001944, the University of Rochester, and the New York State Energy Research and Development Authority. The support of DOE does not constitute an endorsement by DOE of the views expressed in this article.

REFERENCES

1. J. Nuckolls *et al.*, Nature **239**, 139 (1972).
2. S. Atzeni and J. Meyer-ter-Vehn, *The Physics of Inertial Fusion: Beam Plasma Interaction, Hydrodynamics, Hot Dense Matter*, International Series of Monographs on Physics (Clarendon Press, Oxford, 2004).
3. W. L. Kruer *et al.*, Phys. Plasmas **3**, 382 (1996).
4. C. J. Randall, J. R. Albritton, and J. J. Thomson, Phys. Fluids **24**, 1474 (1981).
5. W. Seka, D. H. Edgell, J. P. Knauer, J. F. Myatt, A. V. Maximov, R. W. Short, T. C. Sangster, C. Stoeckl, R. E. Bahr, R. S. Craxton, J. A. Delettrez, V. N. Goncharov, I. V. Igumenshchev, and D. Shvarts, Phys. Plasmas **15**, 056312 (2008).
6. I. V. Igumenshchev, W. Seka, D. H. Edgell, D. T. Michel, D. H. Froula, V. N. Goncharov, R. S. Craxton, L. Divol, R. Epstein, R. Follett, J. H. Kelly, T. Z. Kosc, A. V. Maximov, R. L. McCrory, D. D. Meyerhofer, P. Michel, J. F. Myatt, T. C. Sangster, A. Shvydky, S. Skupsky, and C. Stoeckl, Phys. Plasmas **19**, 056314 (2012).
7. D. H. Froula, I. V. Igumenshchev, D. T. Michel, D. H. Edgell, R. Follett, V. Yu. Glebov, V. N. Goncharov, J. Kwiatkowski, F. J. Marshall, P. B. Radha, W. Seka, C. Sorce, S. Stagnitto, C. Stoeckl, and T. C. Sangster, Phys. Rev. Lett. **108**, 125003 (2012).
8. R. K. Kirkwood *et al.*, Phys. Rev. Lett. **76**, 2065 (1996).
9. W. Seka, H. A. Baldis, J. Fuchs, S. P. Regan, D. D. Meyerhofer, C. Stoeckl, B. Yaakobi, R. S. Craxton, and R. W. Short, Phys. Rev. Lett. **89**, 175002 (2002).
10. S. H. Glenzer *et al.*, Science **327**, 1228 (2010).

11. N. B. Meezan *et al.*, Phys. Plasmas **17**, 056304 (2010).

12. P. Michel *et al.*, Phys. Plasmas **17**, 056305 (2010).

13. P. Michel *et al.*, Phys. Plasmas **20**, 056308 (2013).

14. D. T. Michel, S. Depierreux, C. Stenz, V. Tassin, and C. Labaune, Phys. Rev. Lett. **104**, 255001 (2010).

15. D. Turnbull *et al.*, Phys. Rev. Lett. **114**, 125001 (2015).

16. I. V. Igumenshchev, D. H. Edgell, V. N. Goncharov, J. A. Delettrez, A. V. Maximov, J. F. Myatt, W. Seka, A. Shvydky, S. Skupsky, and C. Stoeckl, Phys. Plasmas **17**, 122708 (2010).

17. D. T. Michel, V. N. Goncharov, I. V. Igumenshchev, R. Epstein, and D. H. Froula, Phys. Rev. Lett. **111**, 245005 (2013).

18. S. Skupsky, J. A. Marozas, R. S. Craxton, R. Betti, T. J. B. Collins, J. A. Delettrez, V. N. Goncharov, P. W. McKenty, P. B. Radha, T. R. Boehly, J. P. Knauer, F. J. Marshall, D. R. Harding, J. D. Kilkenny, D. D. Meyerhofer, T. C. Sangster, and R. L. McCrory, Phys. Plasmas **11**, 2763 (2004).

19. D. H. Edgell, P. B. Radha, D. H. Froula, V. N. Goncharov, I. V. Igumenshchev, J. F. Myatt, and W. Seka, presented at the 42nd Annual Anomalous Conference, Key West, FL, 25–29 June 2012.

20. J. A. Marozas, T. J. B. Collins, P. W. McKenty, and J. D. Zuegel, presented at the 57th Annual Meeting of the APS Division of Plasma Physics, Savannah, GA, 16–20 November 2015.

21. P. B. Radha, T. J. B. Collins, J. A. Delettrez, Y. Elbaz, R. Epstein, V. Yu. Glebov, V. N. Goncharov, R. L. Keck, J. P. Knauer, J. A. Marozas, F. J. Marshall, R. L. McCrory, P. W. McKenty, D. D. Meyerhofer, S. P. Regan, T. C. Sangster, W. Seka, D. Shvarts, S. Skupsky, Y. Srebro, and C. Stoeckl, Phys. Plasmas **12**, 056307 (2005).

22. D. Cao, G. Moses, and J. Delettrez, Phys. Plasmas **22**, 082308 (2015).

23. J. A. Marozas, T. J. B. Collins, J. D. Zuegel, P. B. Radha, F. J. Marshall, and W. Seka, presented at the 44th Annual Anomalous Absorption Conference, Estes Park, CO, 8–13 June 2014.

24. T. R. Boehly, V. A. Smalyuk, D. D. Meyerhofer, J. P. Knauer, D. K. Bradley, R. S. Craxton, M. J. Guardalben, S. Skupsky, and T. J. Kessler, J. Appl. Phys. **85**, 3444 (1999).

25. T. R. Boehly, D. L. Brown, R. S. Craxton, R. L. Keck, J. P. Knauer, J. H. Kelly, T. J. Kessler, S. A. Kumpan, S. J. Loucks, S. A. Letzring, F. J. Marshall, R. L. McCrory, S. F. B. Morse, W. Seka, J. M. Soures, and C. P. Verdon, Opt. Commun. **133**, 495 (1997).

26. E. M. Campbell and W. J. Hogan, Plasma Phys. Control. Fusion **41**, B39 (1999).

27. P. B. Radha, J. A. Marozas, F. J. Marshall, A. Shvydky, T. J. B. Collins, V. N. Goncharov, R. L. McCrory, P. W. McKenty, D. D. Meyerhofer, T. C. Sangster, and S. Skupsky, Phys. Plasmas **19**, 082704 (2012).

28. Y. Lin, T. J. Kessler, and G. N. Lawrence, Opt. Lett. **21**, 1703 (1996).

29. S. Skupsky, R. W. Short, T. Kessler, R. S. Craxton, S. Letzring, and J. M. Soures, J. Appl. Phys. **66**, 3456 (1989).

30. M. Hohenberger, P. B. Radha, J. F. Myatt, S. LePape, J. A. Marozas, F. J. Marshall, D. T. Michel, S. P. Regan, W. Seka, A. Shvydky, T. C. Sangster, J. W. Bates, R. Betti, T. R. Boehly, M. J. Bonino, D. T. Casey, T. J. B. Collins, R. S. Craxton, J. A. Delettrez, D. H. Edgell, R. Epstein, G. Fiksel, P. Fitzsimmons, J. A. Frenje, D. H. Froula, V. N. Goncharov, D. R. Harding, D. H. Kalantar, M. Karasik, T. J. Kessler, J. D. Kilkenny, J. P. Knauer, C. Kurz, M. Lafon, K. N. LaFortune, B. J. MacGowan, A. J. Mackinnon, A. G. MacPhee, R. L. McCrory, P. W. McKenty, J. F. Meeker, D. D. Meyerhofer, S. R. Nagel, A. Nikroo, S. Obenschain, R. D. Petrasso, J. E. Ralph, H. G. Rinderknecht, M. J. Rosenberg, A. J. Schmitt, R. J. Wallace, J. Weaver, C. Widmayer, S. Skupsky, A. A. Solodov, C. Stoeckl, B. Yaakobi, and J. D. Zuegel, Phys. Plasmas **22**, 056308 (2015).

31. D. K. Bradley, P. M. Bell, J. D. Kilkenny, R. Hanks, O. Landen, P. A. Jaanimagi, P. W. McKenty, and C. P. Verdon, Rev. Sci. Instrum. **63**, 4813 (1992).

32. D. K. Bradley *et al.*, Rev. Sci. Instrum. **66**, 716 (1995).

33. D. T. Michel, A. K. Davis, W. Armstrong, R. Bahr, R. Epstein, V. N. Goncharov, M. Hohenberger, I. V. Igumenshchev, R. Jungquist, D. D. Meyerhofer, P. B. Radha, T. C. Sangster, C. Sorce, and D. H. Froula, High Power Laser Science and Engineering **3**, e19 (2015).

34. D. T. Michel, C. Sorce, R. Epstein, N. Whiting, I. V. Igumenshchev, R. Jungquist, and D. H. Froula, Rev. Sci. Instrum. **83**, 10E530 (2012).

35. A. K. Davis, D. T. Michel, S. X. Hu, R. S. Craxton, R. Epstein, V. N. Goncharov, I. V. Igumenshchev, T. C. Sangster, and D. H. Froula, Rev. Sci. Instrum. **85**, 11D616 (2014).

36. J. J. MacFarlane *et al.*, High Energy Density Phys. **3**, 181 (2007).

37. B. I. Bennett, J. D. Johnson, G. I. Kerley, and G. T. Rood, Los Alamos National Laboratory, Los Alamos, NM, Report LA-7130 (1978).

38. H. Takabe and T. Nishikawa, J. Quant. Spectrosc. Radiat. Transf. **51**, 379 (1994).

39. P. B. Radha, M. Hohenberger, D. H. Edgell, J. A. Marozas, F. J. Marshall, D. T. Michel, M. J. Rosenberg, W. Seka, A. Shvydky, T. R. Boehly, T. J. B. Collins, E. M. Campbell, R. S. Craxton, J. A. Delettrez, S. N. Dixit, J. A. Frenje, D. H. Froula, V. N. Goncharov, S. X. Hu, J. P. Knauer, R. L. McCrory, P. W. McKenty, D. D. Meyerhofer, J. F. Myatt, R. D. Petrasso, S. P. Regan, T. C. Sangster, H. Sio, S. Skupsky, and A. Zylstra, Phys. Plasmas **23**, 056305 (2015).